Smart Materials and Structures

PURPOSE-LED PUBLISHING™

PAPER

Approximate field measures for ionic polymer-metal composite materials and a simplified order-of-magnitude actuator model

To cite this article: Zakai J Olsen and Kwang J Kim 2022 *Smart Mater. Struct.* **31** 025029

IOP Publishing Smart Materials and Structures
Smart Mater. Struct. **31** (2022) 025029 (14pp) https://doi.org/10.1088/1361-665X/ac4876

Approximate field measures for ionic polymer-metal composite materials and a simplified order-of-magnitude actuator model

Zakai J Olsen and Kwang J Kim*

Active Materials and Smart Living (AMSL) Lab, Department of Mechanical Engineering, University of Nevada Las Vegas, Las Vegas, NV, United States of America

E-mail: kwang.kim@unlv.edu

Received 24 November 2021, revised 28 December 2021
Accepted for publication 4 January 2022
Published 20 January 2022

Abstract

As the field of soft robotics grows and new applications for this technology are discovered, the use of simplified models for the soft actuators found in these devices will be critical. In this study we explore arguments based on the magnitude of field gradients that arise in the ionic polymer-metal composite (IPMC) under large applied voltages and their use for approximating measures of the fields inside the polymer. Using the order-of-magnitude based arguments provides exceptional results for quantifying the field measures of maximum ionic concentration and electric potential within the bulk of the polymer. These measures are leveraged to reconstruct the fields themselves in such a way that the internal bending moments generated inside the actuator may be approximated. With the internal moments, a simplified kinematic model may be used to formulate the steady-state actuator response of the IPMC. This actuator model shows a great deal of accuracy as compared to a full multiphysics model, and we discuss the prospects for future development of this model to account for dynamic actuation.

Keywords: multiphysics modeling, soft-robotics, biomimetics, ionic polymer-metal composites, electroactive polymers

(Some figures may appear in colour only in the online journal)

1. Introduction

The ionic polymer-metal composites (IPMC) is a type of electroactive polymer based smart material which exhibits both electromechanical (actuation) and mechanoelectrical (sensing) behaviors [1–3]. These materials find applications among the fields of robotics, biomimetics, and soft-robotics due to their low voltage inputs (0.5–2 V), large deformations, relatively fast response speed (0.1–5 Hz), and capability to operate underwater [4–6]. The IPMC is fabricated from a thin membrane of ion conducting polymer composited with surface electrodes [7–13].

The transduction phenomenon of the IPMC is explained by the existence of fixed charges attached to the polymer backbone and mobile charges within the interstitial structure of the membrane. Mobile ions migrate under the application of an externally applied voltage, dragging with them solvent molecules [14–20]. This redistribution of ions and generates an osmotic pressure that works along with electrostatic forces to deforms the IPMC [3, 21–25]. Conversely, mechanically deforming the material creates a pressure gradient

* Author to whom any correspondence should be addressed.

in the porous membrane and advective redistribution of solvent and ionic species which in turn establishes a charge imbalance and detectable electrical signals in the electrodes [3, 26–30].

The current state of modeling IPMC actuators is expansive, encompassing many methodologies and techniques to formulate models reaching all scales of complexity. Some works use the microstructure of the ionic polymer as a basis for developing the modeling framework [23, 31], while others leverage transport equations, such as the Poisson-Nernst-Planck (PNP) system, with classic structural mechanics to create a multiphysics model of IPMC transduction [14, 32–38].

More recent works leverage continuum thermodynamics to construct models that are derivable from potential functions [24, 39–42]. Some recent works focus on a thermodynamically consistent formulations and examine more complex behaviors due to porosity, steric effects, layered microstructure, and the nature of back relaxation phenomena [24, 43–45]. What all of these have in common is their goal of coupling the electrochemistry of migrating ionic species to the mechanical deformation of a solid structure. In this study we use a slightly modified form of the classic PNP and structural mechanics formulation. These equations are cast in the nondimensional formulation recently developed by the present authors [44]. Using this multiphysics model as a basis, we look to develop rough approximations to the electrochemical fields using arguments based on the orders of magnitude of the relevant field gradients. These measures are leveraged to reconstruct approximations to the fields to be used in a simplified kinematic model for the steady-state deformation of the IPMC.

2. An order-of-magnitude model for the IPMC actuator

Here we develop order-of-magnitude (OoM) estimates of key values characterizing the steady-state electrochemical fields of IPMC materials. These measures are then leveraged to construct a simplified actuator model in an attempt to formulate an estimation of the steady-state tip displacement and angle. The goal of these efforts is to establish a closed-form mathematical model to estimate the performance of a cantilever IPMC that may be used in control systems for IPMC enabled soft-robotics. In particular, we construct a model that effectively accounts for both forward displacement and back-relaxation to achieve the steady-state deformation of the IPMC strip, and we discuss extensions of the model for dynamic actuation and sensing as avenues of future study.

2.1. Estimating maximum ion concentration and bulk electric potential

We leverage a simplified multiphysics framework than that found in [44], in which we neglect the effects of the interstitial pore fluid, coupled solvent-ion transport, and consider lossless electrodes. The resulting equations form the PNP equations coupled to a linear elastic model with the modified strain tensor; a modeling framework used throughout literature [32, 33, 35, 46, 47]. We remark on a few of the notational aspects of the model as derived in [44]. Firstly, underbars are used to denote the tensor rank of a quantity. For instance, the scalar molar concentration (rank-0 tensor) is written as c, the vector of the displacement field with a single underbar (rank-1 tensor) as $\underline{u}$, and the Cauchy stress tensor (rank-2 tensor) as $\underline{\underline{\sigma}}$. During the derivation the governing equations are nondimensionalized. In this process the use of an accent hat is used to denote the dimensionless quantity (e.g. the nondimensional stress tensor is written as $\widehat{\underline{\underline{\sigma}}}$). Lastly, in the nondimensionalization process the physical constants are collected into dimensionless groups (Π-groups). Those Π-groups relevant to this model are provided in table 1.

Table 1. Dimensionless groups with descriptions and shorthand names.

Dimensionless group	Physical description	Shorthand name
$\Pi_6 = \dfrac{l}{h}$	Aspect ratio of IPMC as length vs thickness	Aspect ratio
$\Pi_7 = \dfrac{\phi_{a,c}}{\phi_{th}} = \dfrac{\mathcal{F}\phi_{a,c}}{RT}$	Driving input for IPMC actuator/electromigration	Driving potential
$\Pi_8 = \dfrac{\epsilon\left(\dfrac{\phi_{th}}{h}\right)^2}{\mathcal{C}_E}$	Stress contribution due to electrostatic/Maxwell tensor	Maxwell number
$\Pi_9 = \dfrac{RTc_{+,0}}{\mathcal{C}_E}$	Stress contribution due to osmotic pressure	Osmotic number
$\Pi_{10} = \mathcal{C}_\nu$	Poisson ratio of linear elastic material	Poisson ratio
$\Pi_{15} = z_+$	Charge number for mobile ionic species	Mobile charge number
$\Pi_{19} = \dfrac{h}{\lambda_d} = h\mathcal{F}\sqrt{\dfrac{z_+^2 c_{+,0}}{\epsilon RT}}$	Ratio of ionomer thickness to Debye screening length	Reciprocal double layer

The Driving Potential is a dimensionless measure of the actuation voltage magnitude, and is formed by the characteristic applied potential, $\phi_{a,c}$, and the thermal voltage, ϕ_{th}. Values for the remaining material properties and physical constants used to construct these dimensionless Π-groups are provided in the appendix in table 2. The nondimensionalized governing equations, as rendered at steady state, are obtained as:

$$-\widehat{\nabla}\cdot\widehat{\nabla}\hat{\phi} = \frac{\Pi_{19}^2}{\Pi_{15}}(\hat{c}-1) \tag{1a}$$

$$\widehat{\nabla}\cdot\left(\widehat{\nabla}\hat{c} + \Pi_{15}\hat{c}\widehat{\nabla}\hat{\phi}\right) = 0 \tag{1b}$$

$$\widehat{\nabla}\cdot\underline{\hat{\sigma}}^T = 0,\quad \underline{\hat{\sigma}} = \underline{\hat{\sigma}}_{\text{mech}} + \underline{\hat{\sigma}}_{\text{ion}} + \underline{\hat{\sigma}}_{\text{pol}} \tag{1c}$$

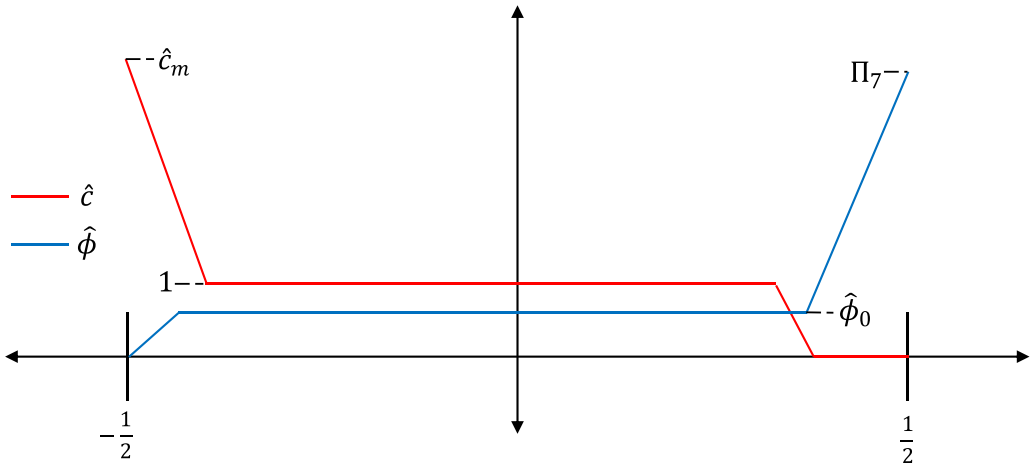

Figure 1. Illustration of concentraiton and electric potential fields in IPMC membranes. The simplified graphic above highlights the relations between maximum and bulk concentrations, as well as driving potential and bulk potential. The illustration greatly simplifies the functional form of these fields but captures the general behavior for constructing approximations for these key field values.

$$\underline{\underline{\hat{\sigma}}}_{\text{mech}} = \frac{1}{1+\Pi_{10}}\left(\frac{\Pi_{10}}{1-2\Pi_{10}} tr\left(\underline{\underline{E}}^*\right)\underline{\underline{I}} + \underline{\underline{E}}^*\right) \tag{1d}$$

$$\underline{\hat{\sigma}}_{\text{ion}} = \Pi_9\left(1-\hat{c}\right)\underline{I} \tag{1e}$$

$$\underline{\hat{\sigma}}_{\text{pol}} = \Pi_8\left(\underline{\hat{d}}\otimes\underline{\hat{d}} - \frac{1}{2}\left(\underline{\hat{d}}\cdot\underline{\hat{d}}\right)\underline{\underline{I}}\right) \tag{1f}$$

$$\underline{\underline{E}}^* = \underline{\underline{\varepsilon}} + \frac{1}{2}\underline{\underline{\omega}}^T\underline{\underline{\omega}} \tag{1g}$$

$$\underline{\underline{\varepsilon}} = \frac{1}{2}\Pi_6\left(\widehat{\nabla}\underline{\hat{u}} + \left(\widehat{\nabla}\underline{\hat{u}}\right)^T\right) \tag{1h}$$

$$\underline{\underline{\omega}} = \frac{1}{2}\Pi_6\left(\widehat{\nabla}\underline{\hat{u}} - \left(\widehat{\nabla}\underline{\hat{u}}\right)^T\right). \tag{1i}$$

Note the use of a partially linearized Green-Lagrange strain tensor, $\underline{\underline{E}}^*$, which accounts for a small degree of rotational deformation in the kinematic model [48]. These equations can be interpreted as follows: Poisson's equation (1*a*), Nernst-Planck equation (1*b*), mechanical equilibrium and stress decomposition (1*c*), stress components (1*d*)–(1*f*), Green-Lagrange strain (1*g*), infinitesimal strain tensor (1*h*), infinitesimal rotation tensor (1*i*). Additionally, we have a relationship between the dimensionless groups Π_8, Π_9, Π_{15}, and Π_{19} given below [44]

$$\Pi_8 = \Pi_9\left(\frac{\Pi_{15}}{\Pi_{19}}\right)^2. \tag{2}$$

This analysis primarily leverages the cation flux (Nernst-Planck) equation. The Nernst-Planck equation governs the electrokinetic phenomena of the mobile ions under the influence of diffusion and electromigration. In the case of an IPMC, the mobile ionic species are bound within the membrane, and hence along the external surfaces of the membrane an ion blocking condition is enforced. At steady state, the Nernst-Planck equation, when combined with the ion blocking condition, relates the gradients in the concentration and electric potential fields. Upon integration and application of the ion blocking condition we are left with

$$\widehat{\nabla}\hat{c} + \Pi_{15}\hat{c}\widehat{\nabla}\hat{\phi} = 0. \tag{3}$$

Now, invoking the knowledge that at high electric potentials the steepest gradients in electric potential and cation concentration occur at the anode (+) and cathode (−), respectively, and constitute the majority of the change in these two fields. The notion of anode and cathode are somewhat ambiguous in a dimensionless setting, but we retain the convention as if the applied potential were positive on the upper electrode and we have a mobile cationic species. These gradients occur over short length scales near the polymer-electrode interface, and these interface regions are what we call the boundary layers at each electrode.

At the anode, the electric potential rises from some intermediate value $\hat{\phi}_0$ up to the dimensionless applied potential Π_7, while at the cathode it falls to zero. Conversely, at the cathode the ionic concentration rises from its bulk value of 1 up to some maximum concentration $\hat{c}_m$ and at the anode falls to zero, representing full depletion of the species. A schematic of these fields is provided in figure 1.

Note that equation (3) applies at all points within the membrane and may be read as a relationship between the gradients in the concentration and potential fields. It is observed that with increasing applied potential, large Π_7, the gradients become asymmetric and both fields exhibit a very large gradient at one electrode in particular, which electrode depends on the polarity of the mobile ion and the applied voltage, but here it may be assumed that concentration rises at the cathode while the potential rises at the anode. Herein lies the key to establishing the approximations for maximum concentration and bulk potential. For the sake of exploration, we look

leverage equation (3) and compare the large gradients in concentration and electric potential which occur at opposing electrodes. Hence, we relate the magnitude of large gradients in concentration at the anode with that of the potential at the cathode, i.e.:

$$\left|\widehat{\nabla}\hat{c}\right|_{-} = \left|\Pi_{15}\hat{c}\widehat{\nabla}\hat{\phi}\right|_{+}. \tag{4}$$

At the anode the concentration is linearized with respect to the bulk value. The gradient terms are approximated using the secant curve rising from the bulk to maximum value of the concentration or potential, and the distance over which this increase from the bulk occurs is assumed to be equal at the cathode and anode. With this, we formulate an equation relating the maximum ionic concentration and the bulk electric potential

$$\hat{c}_m - 1 = \left(\Pi_7 - \hat{\phi}_0\right)\Pi_{15}. \tag{5}$$

This serves as one equation for two unknowns, the maximum concentration and bulk potential. To obtain another equation we look at just the cathode region. Equation (3) applies at any point within the membrane, and hence we use this relation again for the cathode region. Here we again use a secant curve to approximate the gradients, but the concentration in the second term of equation (3) is computed as an average concentration, $\langle\hat{c}\rangle_{-}$, within this cathode boundary layer. This value can be determined by assuming a functional form for the concentration rise in the boundary layer up from the bulk value of 1 and is determined next

$$\begin{aligned}\left|\widehat{\nabla}\hat{c}\right|_{-} &= \left|\Pi_{15}\hat{c}\widehat{\nabla}\hat{\phi}\right|_{-}\\ \hat{c}_m - 1 &= \Pi_{15}\langle\hat{c}\rangle_{-}\hat{\phi}_0.\end{aligned} \tag{6}$$

For the sake of obtaining rough estimation, we assume the concentration profile is approximately exponential to calculate the average cation concentration within the cathode boundary layer

$$\langle\hat{c}\rangle_{-} = \frac{\hat{c}_m - 1}{\ln\left(\hat{c}_m\right)}. \tag{7}$$

Combining these results, we obtain equations governing the maximum concentration and bulk potential, which are our key OoM measures that constitute the basis for constructing a simplified actuator model

$$\hat{c}_m + \ln\left(\hat{c}_m\right) = 1 + \Pi_7\Pi_{15}. \tag{8a}$$

$$\hat{\phi}_0 = \left(1 - \frac{\hat{c}_m - 1}{\Pi_7\Pi_{15}}\right)\Pi_7. \tag{8b}$$

The solution of the concentration equation is given by the principal branch of the Lambert W function and hence we obtain the desired approximations below, subscripted with 1 to denote the first approximation

$$\left(\hat{c}_m\right)_1 = W_0\left(\exp\left(1 + \Pi_7\Pi_{15}\right)\right). \tag{9a}$$

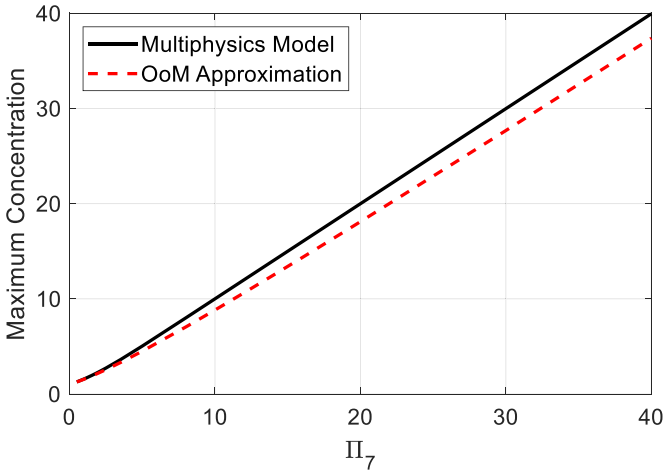

Figure 2. Comparison of multiphysics and OoM model for maximum concentration. The order-of-magnitude approximation using the Lambert W function is compared against the multiphysics model for the maximum concentration. There is a clear underestimation in the OoM approximation, but it captures the linearly dominated feature seen in the multiphysics model.

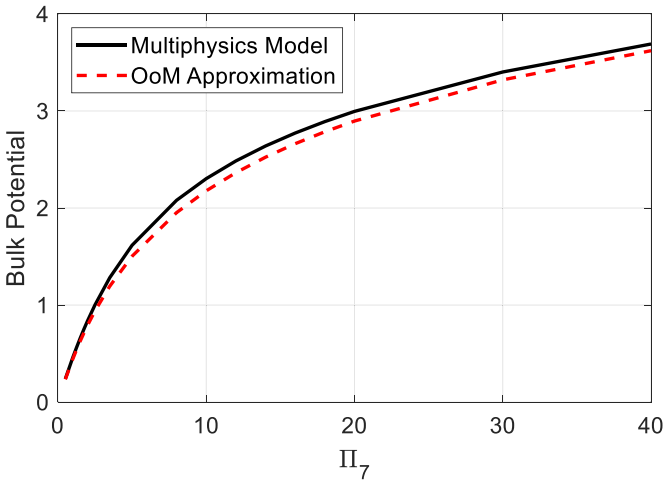

Figure 3. Comparison of multiphysics and OoM model for bulk potential. The order-of-magnitude approximation using the Lambert W function is compared against the multiphysics model for the bulk potential. The OoM approximation effectively captures the general shape of the bulk potential as a function of driving potential, but there is a small underestimation in the approximated value versus the multiphysics model.

$$\left(\hat{\phi}_0\right)_1 = \left(1 - \frac{W_0\left(\exp\left(1 + \Pi_7\Pi_{15}\right)\right) - 1}{\Pi_7\Pi_{15}}\right)\Pi_7. \tag{9b}$$

The result of these equations across a range of applied potentials are provided in figures 2 and 3 for the maximum concentration and bulk potential, respectively. We first examine some limiting behaviors of these measures. For large values of Π_7 we can leverage the asymptotic expansion for the Lambert W function which, retaining only the first two terms, is given below [49]

$$W_0(x) \approx \ln(x) - \ln(\ln(x)) + O\left(\frac{\ln(\ln(x))}{\ln(x)}\right). \tag{10}$$

Hence, we may formulate the asymptotic forms of the maximum concentration and bulk potential (superscript ∞) as provided below.

$$(\hat{c}_m)_1^{\infty} \approx 1 + \Pi_7\Pi_{15} - \ln(1 + \Pi_7\Pi_{15}) \tag{11a}$$

$$\left(\hat{\phi}_0\right)_1^{\infty} \approx \frac{\ln(1+\Pi_7\Pi_{15})}{\Pi_7\Pi_{15}}\Pi_7 = \frac{\ln(1+\Pi_7\Pi_{15})}{\Pi_{15}}. \tag{11b}$$

For small values of Π_7 (superscript 0) we form the Taylor series expansion of the maximum concentration and bulk potential about $\Pi_7 = 0$.

$$(\hat{c}_m)_1^0 \approx \hat{c}_m(0) + \left.\frac{d\hat{c}_m}{d\Pi_7}\right|_0 \Pi_7 = 1 + \frac{1}{2}\Pi_7\Pi_{15} \tag{12a}$$

$$\left(\hat{\phi}_0\right)_1^0 \approx \hat{\phi}_0(0) + \frac{d\hat{\phi}_0}{d\Pi_7}|_0\Pi_7 = \frac{\Pi_7}{2}. \tag{12b}$$

We find that the above expansions for small values of Π_7 agree with our intuition of the low voltage response in the concentration and potential fields. For very low applied voltages the bulk potential approaches half the value of applied potential as $\Pi_7 \to 0$, indicating a symmetric distribution of the ions and potential as would be expected in the linear regime of the multiphysics model. Also note that asymptotic expansion of the concentration and potential correctly capture the behavior at the point $\Pi_7 = 0$ but do not admit Taylor series expansions about this point that correctly capture the linear behavior of the measures as derived from equation (9). That is to say, equation (11) capture the approximate measures at $\Pi_7 = 0$ (i.e. $\hat{c}_m = 1$, $\hat{\phi}_0 = 0$), but their Taylor series expansions about $\Pi_7 = 0$ fail to capture the linear response found in equation (12) about this point.

Using the approximations in equation (9) we find that these results capture the qualitative behavior of the respective measures, but under-estimate the amplitude of both the maximum concentration and bulk potential (see figure 4). Hence, we now seek to formulate a correction of these approximations to compensate for this behavior.

The simplest adjustment we may make it to assume that at higher applied voltages the electric potential gradient in equation (5) may be approximated as occurring across the full potential drop of the membrane (i.e. the drop at the anode occurs from $\Pi_7 \to 0$ as opposed to $\Pi_7 \to \hat{\phi}_0$). With all other equations in the previous analysis remaining the same (cathode comparison and average concentration) we obtain the following approximation, subscripted with an * as these approximations aim to provide a correction to the original approximations in equation (9) but are ultimately an intermediate step.

$$(\hat{c}_m)_* = 1 + \Pi_7\Pi_{15} \tag{13a}$$

$$\left(\hat{\phi}_0\right)_* = \frac{\ln(1+\Pi_7\Pi_{15})}{\Pi_{15}}. \tag{13b}$$

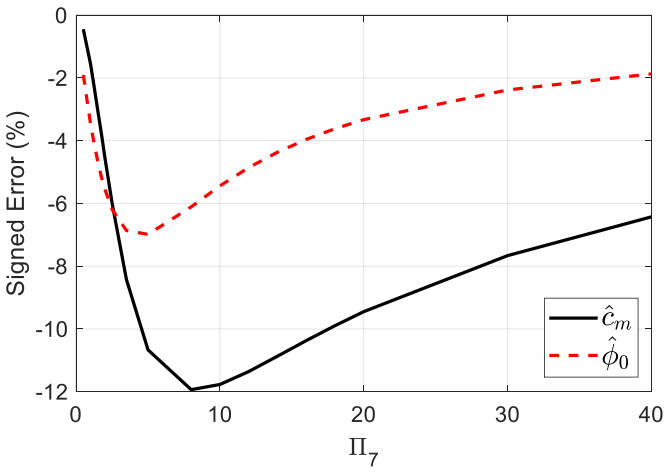

Figure 4. Signed error in OoM approximations using Lambert W function. Both the maximum concentration and bulk potential as calculated from the OoM approximation show underestimations as evident by the negative signed error. The error appears to have an asymptotic decay towards zero within the limited range tested.

Notice we have recaptured the asymptotic behavior for the bulk potential at large applied voltages, and now have a new approximation for the maximum concentration that is found to over-estimate the value as calculated from the multiphysics model. We may use these new estimates to augment the original analysis and construct more accurate approximations. From the small and large Π_7 expansions for the bulk potential we noted that the asymptotic form fails to capture the limiting behavior for small Π_7.

Since the issue in the asymptotic form arises from its inability to capture the behavior at small Π_7 we look to selectively modify this low potential regime. To begin, examine the Taylor series expansion of the asymptotic bulk potential, along with an extend expansion of the Lambert W form:

$$\frac{\ln(1+\Pi_7\Pi_{15})}{\Pi_{15}} \approx \frac{1}{\Pi_{15}}\left(\Pi_7\Pi_{15} - \frac{(\Pi_7\Pi_{15})^2}{2} + \frac{(\Pi_7\Pi_{15})^3}{3} - \frac{(\Pi_7\Pi_{15})^4}{4} + \ldots\right) \tag{14a}$$

$$\left(1 - \frac{W_0(\exp(1+\Pi_7\Pi_{15})) - 1}{\Pi_7\Pi_{15}}\right)\Pi_7 \approx \frac{1}{\Pi_{15}}\left(\frac{\Pi_7\Pi_{15}}{2} - \frac{(\Pi_7\Pi_{15})^2}{16} + \frac{(\Pi_7\Pi_{15})^3}{192} + \frac{(\Pi_7\Pi_{15})^4}{3072} + \ldots\right). \tag{14b}$$

Clearly the asymptotic form predicts a vastly different response for small values of the applied potential. What we propose here is to construct a function whose Taylor series expansion about $\Pi_7 = 0$ is the difference between these two series up to some order n, and add this series to the asymptotic form. The new function that is formed will have the desired Taylor series expansion of the Lambert W form. To retain the approximation power of the asymptotic expansion, we require a function whose Taylor series fits the criteria described, but

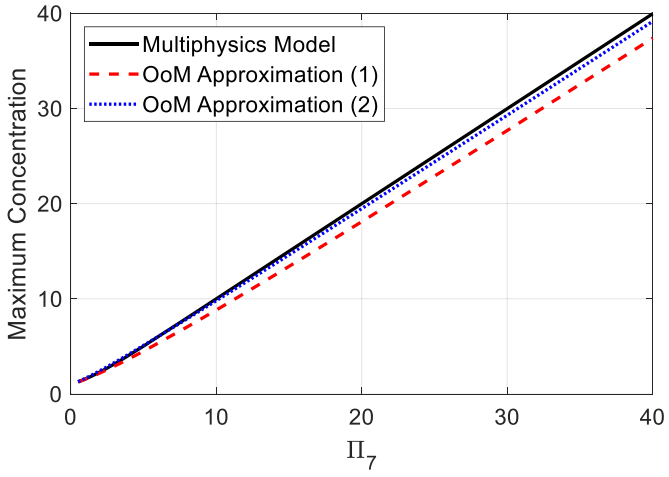

Figure 5. Comparison of new OoM model for maximum concentration. The new OoM model constructed with elementary functions effectively captures the linear dominated features found in the multiphysics model while also correcting most of the underestimation found in the original, Lambert W based approximation.

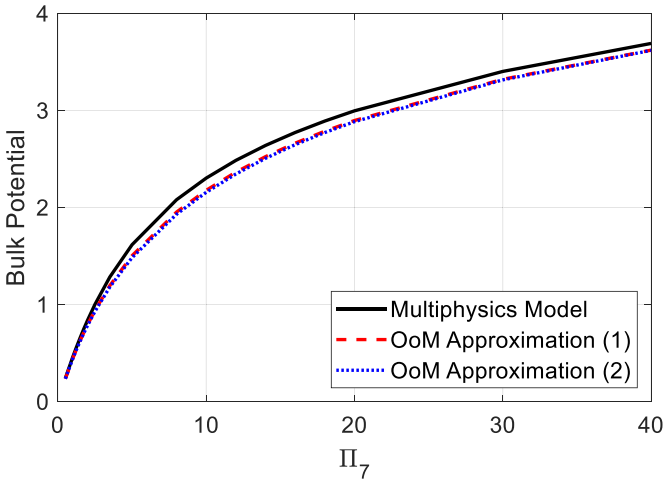

Figure 6. Comparison of new OoM model for bulk potential. The new OoM model constructed with elementary functions effectively captures the result of the Lambert W based approximation without introducing significant loss of accuracy.

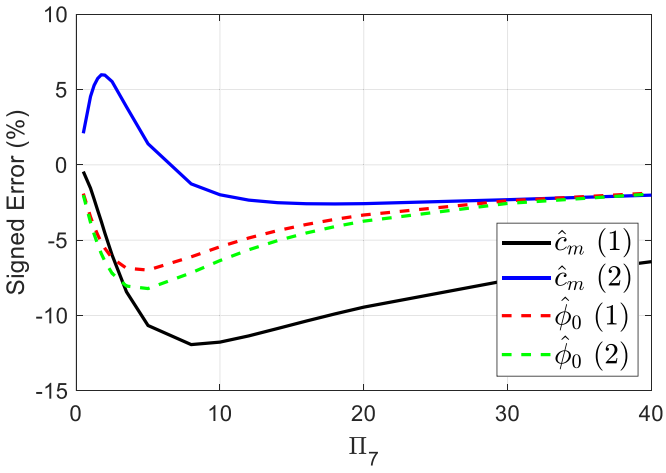

Figure 7. Signed error in OoM approximations using elementary functions. The new OoM estimates for the maximum concentration and bulk potential using elementary functions show improvements over the Lambert W based approximations. For the maximum concentration, we see the new model over-corrected and leads to an overestimation (positive signed error) but with lesser magnitude. For the bulk potential, the general trend in error is the same with only a small increase in peak error while eliminating the nonelementary function.

decays to zero faster than the logarithmic term which dominates in our current approximation for large Π_7. In this regard, we look to utilize a Padé approximant [50], specifically the $[1/2]$ approximant using the difference between Taylor coefficients of the two series above. Hence, we are looking for a rational polynomial $R(x)$ given by:

$$R(x) = \frac{P(x)}{Q(x)} = \frac{p_0 + p_1 x}{1 + q_1 x + q_2 x^2}. \tag{15}$$

Whose Taylor series expansion about $x = 0$ matches the difference in series above up to $O\left(x^4\right)$. We chose low order polynomials to reduce the likelihood of introducing nonphysical singularities in the denominator of equation (15), and we use a non-diagonal Padé approximant so that the function decays to zero appropriately. We formulate this Padé approximant and construct our final approximation for the bulk potential as shown below, subscripted with a 2 as this is our second approximation

$$\left(\hat{\phi}_0\right)_2 = \left(\frac{\ln\left(1 + \Pi_7\Pi_{15}\right)}{\Pi_7\Pi_{15}} - \frac{4}{8 + 7\Pi_7\Pi_{15} + \frac{7}{8}\Pi_7^2\Pi_{15}^2}\right)\Pi_7. \tag{16}$$

Now turning our attention to the maximum concentration, both asymptotic expansion and our new estimate show linearly dominated features for large Π_7 and capture the behavior at the terminal point $\Pi_7 = 0$, and find that a linear combination of the two suffices for balancing the under and over-estimations present in each metric, respectively. Specifically, the arithmetic mean of the two estimates provides an approximation that retains the characteristics of the asymptotic form, properly captures the linear behavior for small Π_7, and effectively corrects the under-estimation of the original approximation at large applied voltages while remaining valid at low applied voltages

$$\left(\hat{c}_m\right)_2 = 1 + \Pi_7\Pi_{15} - \ln\left(\sqrt{1 + \Pi_7\Pi_{15}}\right). \tag{17}$$

We find that this new approximation for the maximum concentration has corrected some of the error found in the initial approximation (see figure 5). Furthermore, these new approximations retain all the characteristics of the original and incur minimal additional error than those using the Lambert W function but are written in terms of elementary functions making them more manageable for future analysis (see figures 6 and 7).

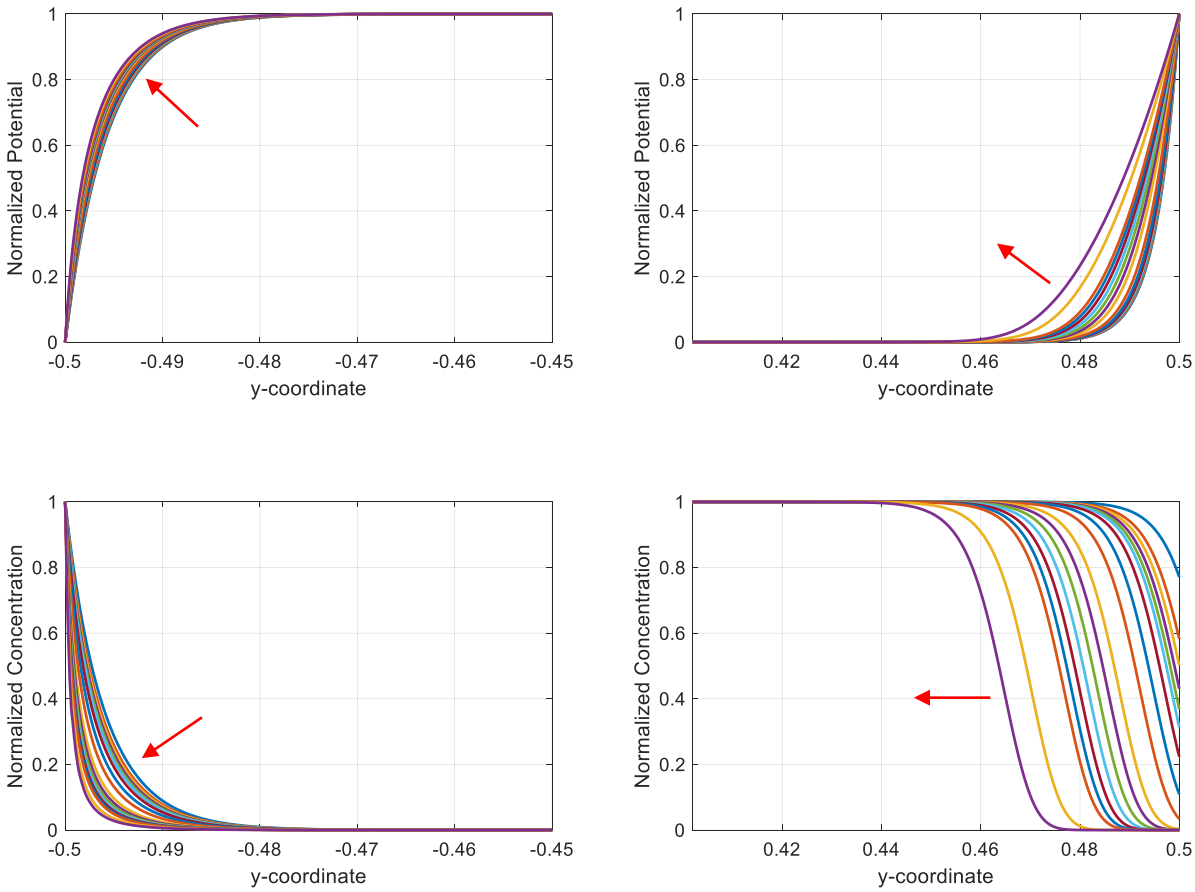

Figure 8. Boundary layer variations with increasing driving potential. The boundary layer for the electric potential (top) and concentration (bottom) evolves with increasing driving potential, sharpening at the cathode (left), where mobile ion accumulation occurs, and widening at the anode (right), where mobile ion depletion occurs. Arrows indicate direction of increasing $\mathbf{\Pi}_7$.

2.2. Evolution of the boundary layers

In the original approximation we implicitly assumed that the boundary layer width over which the gradients occurred were equal at the anode and cathode, which sufficed for our needs to develop OoM approximations for the maximum concentration and bulk potential. Now we construct a more accurate representation of these thicknesses and quantify their relationship to the applied potential and other material properties via the Π-groups. Here we define the boundary layer thickness in the vicinity of either electrode as the region in which the respective field deviates 1% from its value in the bulk membrane.

While this definition of the boundary layer should not be confused with the notion of the mathematical boundary layer used in the method of matched asymptotic expansions (MAE), we may use the definition of the MAE boundary layer to gain some insight into how the physical layers evolve [24, 25, 51]. Under our current dimensionless framework, the boundary layers as defined in MAE are related to the dimensionless groups Π_{15} and Π_{19}

$$\delta_{\mathrm{MAE}} = \frac{\sqrt{\Pi_{15}}}{\Pi_{19}}. \tag{18}$$

To understand how these layers form and evolve with increasing Driving Potential, we leverage the multiphysics model to construct a variety of concentration and electric potential profiles for different values of Π_7, which are provided in figure 8.

First note the fields have been normalized to a range of $[0, 1]$ within their respective boundary layers so the shape of each profile may be more easily compared qualitatively. The overlayed red arrows indicate the direction of evolution with increasing Π_7. We find that at the cathode the profiles evolve significantly less than those at the anode, which are driven by the ionic depletion that occurs at the anode interface. The fields at the cathode and the electric potential at the anode feature exponential-like profiles whereas the cation concentration at the anode has characteristics of a sigmoid curve.

To capture the evolution of these boundary layers we define three parameters, the boundary layer thicknesses Δ_+ and Δ_- at the anode and cathode, respectively, and the transition zone thickness δ_+. The transition zone thickness is a quantity which captures the length over which the sigmoid-like drop in concentration occurs, illustrated in figure 9.

Using the previous definition for the boundary layer, we plot the thickness as a function of Π_7 calculated from the multiphysics model. A preliminary analysis suggests the following models for the boundary layers provide reasonable approximations

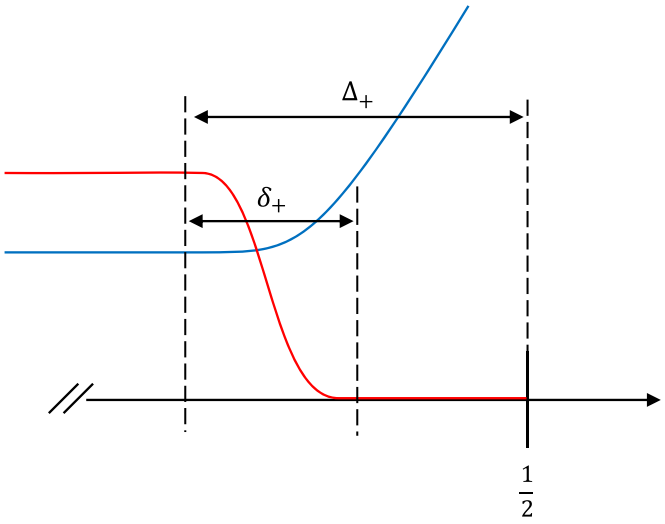

Figure 9. Illustration of characteristic field shapes in vicinity of anode. The electric potential features an exponential-like increase at the anode, while the mobile ion depletes in this region and takes on a sigmoid-like shape.

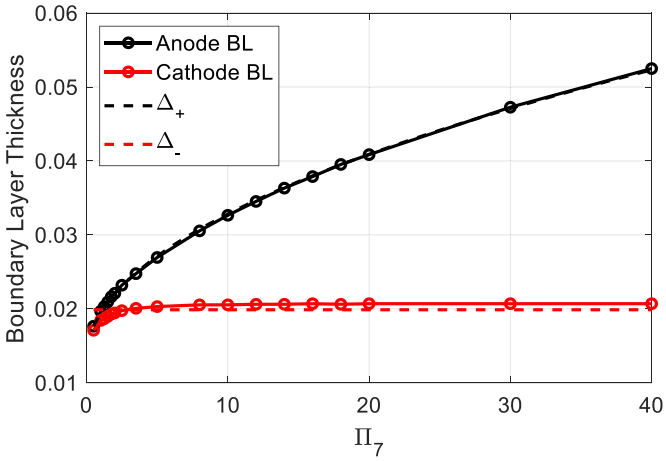

Figure 10. Regression models for anode and cathode boundary layer thickness. The regression models effectively capture the boundary layer variations at the anode and cathode as functions of the driving potential, mobile charge number, and reciprocal double layer.

$$\Delta_+ = \frac{\beta_1\sqrt{\Pi_7\Pi_{15}} + \beta_2}{\Pi_{19}}. \tag{19a}$$

$$\Delta_- = \frac{\beta_3}{\Pi_{19}} \tag{19b}$$

$$\delta_+ = \frac{3}{2}\Delta_-. \tag{19c}$$

These equations capture both the behavior found using the multiphysics model for increasing Π_7 as well as the mathematical notion of the boundary layer from MAE. With these definitions for the boundary layer thicknesses a nonlinear fitting in MATLab finds the regression parameters as $\beta = [1.39\ \ 3.01\ \ 4.49]$, and yields the following results in figure 10.

2.3. Stress resultants and order-of-magnitude deformation

With a model for the boundary layer evolution, we need to establish estimations of the concentration and electric potential within these layers, which will be used to construct the stress resultants within the polymer. Noting that the depletion of the ions near the anode resembles a sigmoid curve across the transition zone δ_+ we leverage the symmetry of this profile and assume an average concentration of $1/2$ within this region. Throughout the remainder of the boundary layer thickness the concentration is assumed to be fully depleted and hence we have an approximate concentration within the anode boundary layer of:

$$\langle\hat{c}\rangle_+ = \frac{1}{2}\frac{\delta_+}{\Delta_+}. \tag{20}$$

We form approximate electric potential gradients at both the anode and cathode using the linear electric potential gradient over boundary layer thicknesses of Δ_- and Δ_+^*, respectively

$$\langle\widehat{\nabla}\hat{\phi}\rangle_- = \alpha\frac{\hat{\phi}_0}{\Delta_-},\ \ \langle\widehat{\nabla}\hat{\phi}\rangle_+ = \alpha\frac{\Pi_7 - \hat{\phi}_0}{\Delta_+^*}. \tag{21a}$$

$$\Delta_+^* = \Delta_+ - \frac{1}{2}\delta_+. \tag{21b}$$

The modified boundary layer thickness Δ_+^* will be used to calculate the electric potential gradient in the vicinity of the anode and is an effective layer thickness for the potential field as the exponential-like rise in the electric potential roughly corresponds with the center of the transition zone of the ion depletion layer (see figures 8 and 9). We have also introduced one free parameter α which is used to correct the underestimation of the electric potential gradients in the model. Using the average gradients above, without the parameter α, there is an over-estimation further away from the polymer-electrode interface and an under-estimation nearer the interface. Because the moment arm for the stress increases as the interface is approached, the Maxwell stress contributions calculated using the above average potential gradients would be under-estimated and hence the parameter α is intended to tune the model to make up for this error and aside from fitting the boundary-layer thickness using the multiphysics model this is the only free parameter used for tuning after the other parameters are determined by dimensionless groups.

We turn to a simplified mechanics model and consider an Euler-Bernoulli beam. The stress resultant moments defined according to classical structural-mechanics formulations, and the contributions to the Cauchy stress tensor via mechanical, ionic, and polarization effects are presented below, in dimensionless form

$$\widehat{\mathcal{M}}_i = \frac{\sigma_c w h^2}{\mathcal{M}_c} \int_{-\frac{1}{2}}^{\frac{1}{2}} \hat{\sigma}_{i,xx} \hat{y} \mathrm{d}\hat{y}. \tag{22a}$$

$$\hat{\sigma}_{\mathrm{mech},xx} = -\mathcal{C}_{\mathcal{B}} \hat{y} \hat{\kappa} \tag{22b}$$

$$\hat{\sigma}_{\mathrm{ion},xx} = \Pi_9 \left(1 - \hat{c}\right) \tag{22c}$$

$$\hat{\sigma}_{\mathrm{pol},xx} = -\frac{\Pi_8}{2} \left(\frac{\mathrm{d}\hat{\phi}}{\mathrm{d}\hat{y}}\right)^2 \tag{22d}$$

wherein $\mathcal{C}_{\mathcal{B}}$ is akin to the flexural rigidity in classic beam theory. We call this quantity the dimensionless beam modulus, which can be expressed as the ratio of the P-wave modulus to the Young's modulus

$$\mathcal{C}_{\mathcal{B}} = \frac{\mathcal{C}_M}{\mathcal{C}_E} = \frac{1 - \Pi_{10}}{\left(1 - 2\Pi_{10}\right)\left(1 + \Pi_{10}\right)}. \tag{23}$$

We define our characteristic resultant moment and obtain the mechanical, ionic, and polarization moments shown below

$$\mathcal{M}_c = \frac{\sigma_c h^2 w}{12}. \tag{24a}$$

$$\widehat{\mathcal{M}}_{\mathrm{mech}} = -\mathcal{C}_{\mathcal{B}} \hat{\kappa} \tag{24b}$$

$$\widehat{\mathcal{M}}_{\mathrm{ion}} = 6\Pi_9 \Delta_+ \left(1 - \Delta_+\right) \left(1 - \langle \hat{c} \rangle_+ - \frac{\Delta_-}{\Delta_+} \frac{1 - \Delta_-}{1 - \Delta_+} \left(1 - \langle \hat{c} \rangle_-\right)\right) \tag{24c}$$

$$\widehat{\mathcal{M}}_{\mathrm{pol}} = 6\Pi_8 \hat{\phi}_0^2 \frac{\alpha - \Delta_-}{\Delta_-} \left(1 - \frac{\Delta_-}{\Delta_+} \frac{\alpha - \Delta_+}{\alpha - \Delta_-} \left(\frac{\Pi_7 - \hat{\phi}_0}{\hat{\phi}_0}\right)^2\right). \tag{24d}$$

A moment balance then requires the summation of these moments equates to zero:

$$\widehat{\mathcal{M}}_{\mathrm{mech}} + \widehat{\mathcal{M}}_{\mathrm{ion}} + \widehat{\mathcal{M}}_{\mathrm{pol}} = 0. \tag{25}$$

And we solve for the dimensionless beam curvature as a function of the external moments from ionic and polarization stresses

$$\hat{\kappa} = \frac{\widehat{\mathcal{M}}_{\mathrm{ion}} + \widehat{\mathcal{M}}_{\mathrm{pol}}}{\mathcal{C}_{\mathcal{B}}}. \tag{26}$$

The dimensionless transverse deformation could be found from the curvature using the linear beam relation. We parametrize the beam by a local axial coordinate s, and consider a fixed clamp boundary condition at $s = 0$. Solving for the deformation of the beam we obtain the following equations for the deformed coordinates, maximum displacement (located at $s = 1$), and steady-state tip angle

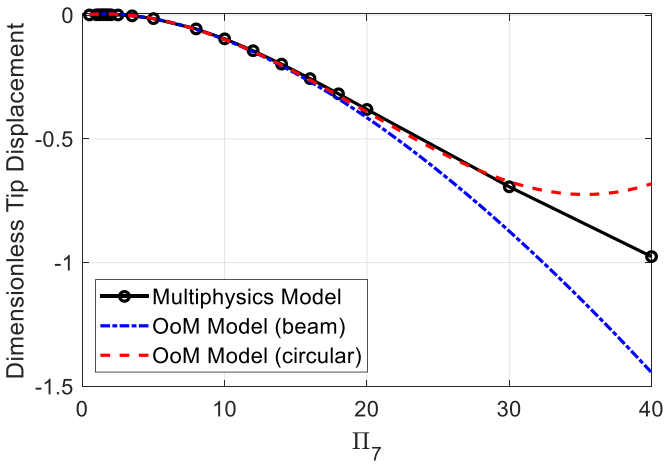

Figure 11. Comparison of multiphysics and OoM model for steady-state tip displacement. The linear beam and circular arc models for the order-of-magnitude IPMC actuator displacement show great agreement with the multiphysics model for driving potentials below ∼12. Above this, the linear beam model significantly deviates from the others. Near a driving potential of ∼22 the circular arc model deviates from the multiphysics model due to the circular arc capturing the extreme nonlinear deformation of IPMCs as they curl backwards on themselves.

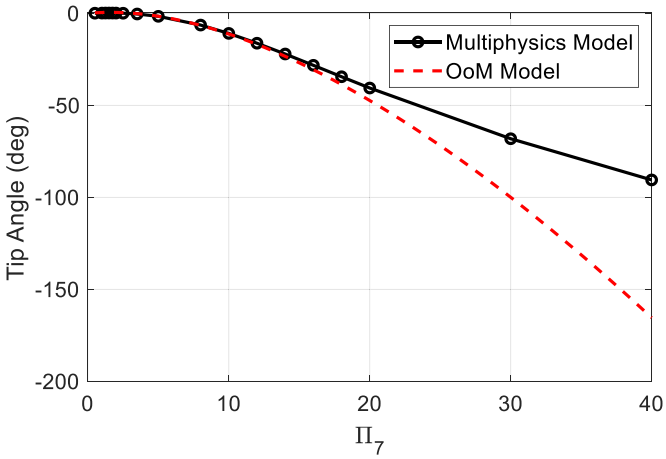

Figure 12. Comparison of multiphysics and OoM model for steady-state bending angle. The linear beam and circular arc models are both calculated from the same curvature, and hence tip angle, which shows good agreement with the multiphysics model for driving potentials below ∼12. Above this, the models being to deviate from one another as the OoM model continues to predict an increasing angle while the multiphysics model, with limited rotational kinematics, begins to plateau and the predicted geometry elongates instead of bends.

$$\hat{x}(s) = \Pi_6 s,\ \hat{y}(s) = \frac{(\Pi_6 s)^2}{2} \hat{\kappa},\ s \in [0,1]. \tag{27a}$$

$$\hat{u}_{x,m} = 0, \hat{u}_{y,m} = \frac{\Pi_6 \hat{\kappa}}{2}, \theta_m = \Pi_6 \hat{\kappa}. \tag{27b}$$

The transverse deformation is calculated under the Euler-Bernoulli beam with an assumption of infinitesimal strain and hence retains no rotational information. If instead we assume that the moment balance calculated above accurately predicts

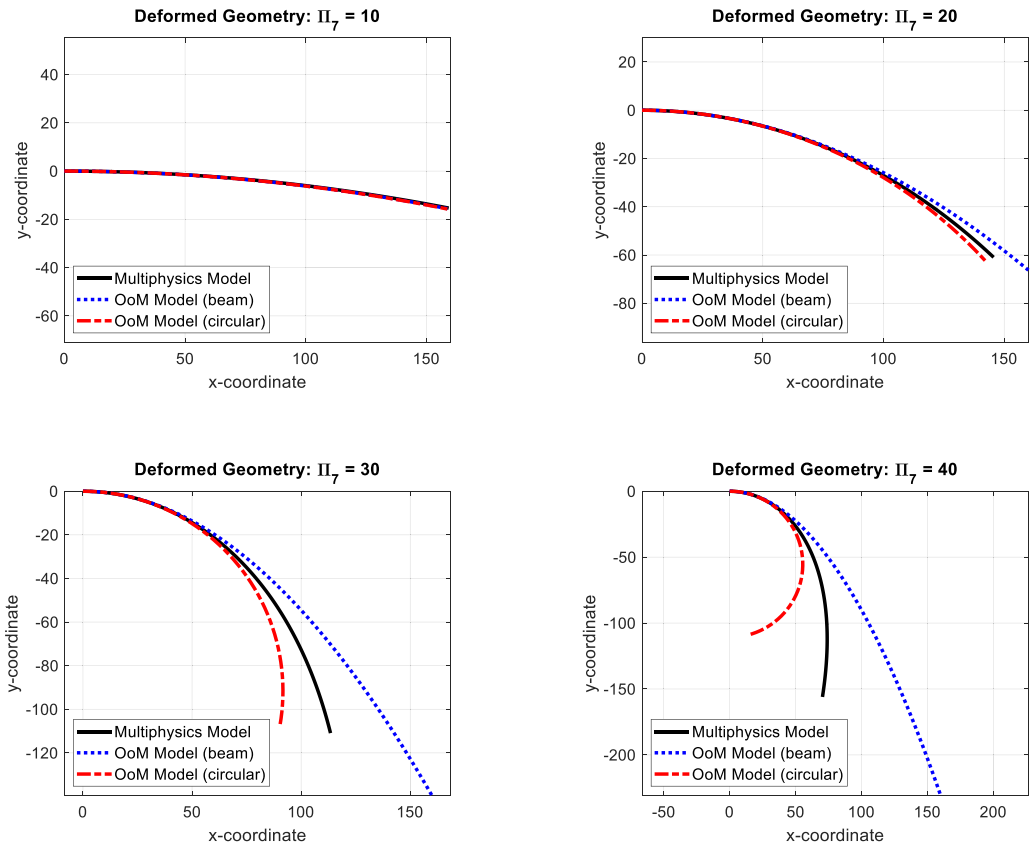

Figure 13. Multiplot of deformed geometry for multiphysics and OoM models. The above subplots demonstrate the capability of the OoM model to accurately calculate the order of magnitude in steady-state deformation of a simplified IPMC actuator. The linearized Euler-Bernoulli beam fails to accurately capture the deformed shape behind even small values of the driving potential (<20) but the circular arc geometry captures the curled shape seen in some IPMC literature.

the dimensionless curvature of the IPMC throughout the range of applied voltages, we can approximate its deformed geometry as a constant curvature arc, parametrized by a local arc-length coordinate s, and obtain the deformed coordinates, maximum displacement, and tip bending angle.

$$\hat{x}(s) = \frac{\sin(\Pi_6\hat{\kappa}s)}{\hat{\kappa}},\ \hat{y}(s) = \frac{1-\cos(\Pi_6\hat{\kappa}s)}{\hat{\kappa}},\ s\in[0,1] \quad (28a)$$

$$\hat{u}_{x,m} = \frac{\sin(\Pi_6\hat{\kappa})}{\Pi_6\hat{\kappa}} - 1, \hat{u}_{y,m} = \frac{1-\cos(\Pi_6\hat{\kappa})}{\Pi_6\hat{\kappa}}, \theta_m = \Pi_6\hat{\kappa}. \quad (28b)$$

The appearance of the Aspect Ratio in the denominator of the displacement is a scaling relation to move from the coordinates, which is scaled by the ionomer thickness, to the displacement, scaled by the IPMC length. Note that the constant curvature equations linearized to those of infinitesimal strain for small angles $\theta = \Pi_6\hat{\kappa}$. This constant curvature approximation neglects any coupling due to finite-strains that may affect the electrochemical fields. Due to the strong through-the-thickness gradients present in IPMC electrochemistry and our previous analysis on the nonlinear kinematics the deformed state should be approximated well and even predict the large bending deformation at high applied voltages for which an infinitesimal strain theory would fail.

A preliminary study finds that $\alpha = 7/25$ yields satisfactory results for approximating the order of magnitude for the tip displacement with a range of applied voltages of $0 < \Pi_7 < 30$, illustrated below in figures 11 and 12. The bending angle strongly deviates after $\sim 15°$, and the OoM model exhibits a large degree of rotational deformation compared to the moderately nonlinear kinematics. This is expected due to the limited amount of bending the moderately nonlinear kinematic model can capture accurately.

We also want to emphasize the reversal of the displacement curve, as predicted by the OoM model, which occurs as the tip angle passes a critical value after which the transverse displacement reaches a maximum and the IPMC strip curls backwards towards the clamped portion. We illustrate in figure 13 the deformed geometry calculated using the multiphysics model with moderately nonlinear kinematics alongside that calculated with the OoM under an assumption the Euler-Bernoulli beam and the constant-curvature arc.

We can more clearly see the breakdown in even the moderately nonlinear kinematics between the voltages of $\Pi_7 = 20$ and $\Pi_7 = 30$. The error incurred during any linearized kinematic model manifests as this characteristic elongation of

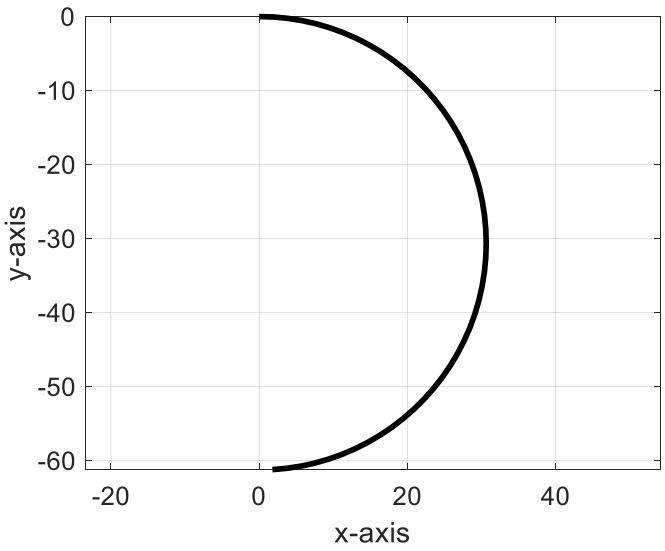

Figure 14. Curled actuator shape for literature comparison. The demonstrated curled actuator shape above utilized the same material properties as in [52], with an adjustment of the fitting parameter $\boldsymbol{\alpha}$ the geometry and degree of actuation is recovered with good accuracy.

the IPMC strip and a failure to reflect rigid body rotation. The OoM model is forced to maintain a fixed length and exhibits the extreme bending angles found at high voltages.

This curled geometry has been captured by similar multiphysics models utilizing finite-strain frameworks, with the same elastic material and ideal dielectric models as presented here [52]. These models also exhibit the exaggerated back-relaxation phenomena that is being captured here. We can compare our OoM model with that literature for these extreme curled shaped. In the work cited, their actuator in its most curled state exhibits a transverse and absolute dimensionless displacement of -0.68 and 1.18, respectively. The current multiphysics model differs from that just cited in that here an osmotic pressure is the source of ionic driven actuation, whereas the cited work uses an eigenstress associated with the accumulation/depletion of ions. Keeping in mind this difference, the OoM model was reformulated with material properties in [52] and the osmotic stress of our multiphysics model was used. Requiring only a change in the parameter $\alpha = 10/13$ to bring the model into agreement, the OoM prediction, with a similar curled actuator geometry (see figure 14), gives values of -0.648 and 1.18 for the transverse and absolute displacements. We find that the fitting parameter α had to decrease to compensate for the material property changes which altered the structure of the boundary layer. In the future, a more sophisticated model for the boundary layer with a material property driven parameter would be beneficial for formulating an OoM model that requires no fitting. Regardless, the resulting deformed shapes between the two models are akin to one another and hence provides support for the OoM model and its representation of these extreme actuator deformations using a constant curvature assumption.

3. Conclusion

Here we have demonstrated the use of OoM arguments in approximating key measures for the chemical concentration and electric potential fields. Using this information, we were able to construct rough approximations of the fields themselves in order to derive closed-form mathematical expressions for the resultant moments for mechanical, osmotic, and Maxwell stresses within the polymer. Using Euler-Bernoulli beam theory and a constant curvature arc we obtain linear and nonlinear kinematic models, respectively, for the steady-state deformation of the cantilever IPMC. The resulting deformation is quantified in terms of the deformed geometry, transverse displacement, and bending angle. Using a constant curvature arc as a kinematic model provides a nonlinear description of the deformation and is capable of representing the curled actuator shapes seen in IPMCs under large applied electric potentials. These OoM modeling results demonstrate a high degree of accuracy in the tip deformation and bending angle when compared with the finite element multiphysics model.

4. Remarks on future development

This model relied on the existence of sharp gradients at both polymer-electrode interfaces to construct the approximate maximum ion concentration and bulk electric potential. In mechanoelectrical transduction these gradients are not as pronounced. In fact, the ionic species exhibits only small changes from its bulk value. As such, the current approach may require modification in order to construct a similar OoM model for the IPMC sensor.

Currently the lone parameter α must be tuned to fit data in order to match the established multiphysics models. Future efforts should establish a link between this parameter and the other Π-groups in the simplified governing equations. In particular, we know that the Osmotic and Maxwell Numbers both have marked effects on the boundary layer formation. One of these parameters may be linked to the Reciprocal Double Layer that is already in the OoM model of the boundary layer thickness, but the remaining Π-group must be accounted for and the fitting parameter linked to these groups for a more complete model. Furthermore, the model is currently only capable of predicting the terminal, steady-state response of the IPMC actuator. Adding an additional parameter to account for the reduced back-relaxation during dynamic actuation, and projection of the static deformed shape onto a set number of modal shapes for the beam may lead to a model that can effectively capture the dynamic actuation performance of IPMC actuators which will find additional use in control models for robotic systems utilizing IPMCs. Regarding this final point, the attractiveness of this new model to control systems is its ability to approximate the deformation with high accuracy using a compact, closed-form expression. With this closed-form expression model-based control schemes may be developed and used on hardware in soft-robotics applications.

The extension of this model for dynamic actuation will be important for this endeavor as many of these robotic systems use IPMC materials as oscillating propulsors.

Data availability statement

The data that support the findings of this study are available upon reasonable request from the authors.

Acknowledgments

The authors acknowledge the partial financial support from the US National Science Foundation (NSF), Partnerships for International Research and Education (PIRE) Program, Grant No. 1545857. Any opinions, findings and conclusions or recommendations expressed in this material are those of the author(s) and do not necessarily reflect the views of the NSF.

Appendix

Table 2. Material properties and physical constants.

Parameter	Value	Physical units	Description
l	40	(mm)	IPMC free length
w	10	(mm)	IPMC width
h	250	(μm)	IPMC thickness
ϵ	6	(mF)	Dielectric constant
$\mathcal{C}_E$	600	(MPa)	Young's modulus
$\mathcal{C}_\nu$	0.45	$(-)$	Poisson ratio
$\mathcal{D}_+$	1×10^{-11}	$\left(\mathrm{m}^2\ \mathrm{s}^{-1}\right)$	Ionic self-diffusivity
z_+	1	$(-)$	Cation charge number
$\mathcal{F}$	96485.332	$\left(\mathrm{C\ mol}^{-1}\right)$	Faraday's constant
R	8.31446262	$\left(\mathrm{J\ mol\ K}^{-1}\right)$	Universal gas constant
T	298.15	(K)	Thermodynamic temperature

ORCID iDs

Zakai J Olsen https://orcid.org/0000-0002-4499-6677
Kwang J Kim https://orcid.org/0000-0003-2134-4964

References

[1] Bar-Cohen Y 2002 Electroactive polymers as artificial muscles: a review *J. Spacecr. Rockets* **39** 822–7
[2] Hines L, Petersen K, Lum G Z and Sitti M 2017 Soft actuators for small-scale robotics *Adv. Mater.* **29** 1603483
[3] Shahinpoor M, Bar-Cohen Y, Simpson J O and Smith J 1998 Ionic polymer-metal composites (IPMCs) as biomimetic sensors, actuators and artificial muscles—a review *Smart Mater. Struct.* **7** R15–R30
[4] Kim K J, Yim W, Paquette J W and Kim D 2007 Ionic polymer-metal composites for underwater operation *J. Intell. Mater. Syst. Struct.* **18** 123–31
[5] Shahinpoor M 1992 Conceptual design, kinematics and dynamics of swimming robotic structures using ionic polymeric gel muscles *Smart Mater. Struct.* **1** 91–94
[6] Yim W, Lee J and Kim K J 2007 An artificial muscle actuator for biomimetic underwater propulsors *Bioinsp. Biomim.* **2** S31–S41
[7] Shahinpoor M and Kim K J 2001 Ionic polymer-metal composites: I. Fundamentals *Smart Mater. Struct.* **10** 819–33
[8] Kim K J 2007 Ionic polymer-metal composite as a new actuator and transducer material *Electroactive Polymers for Robotic Applications* ed K J Kim and S Tadokoro (London: Springer) pp 153–64
[9] Bahramzadeh Y and Shahinpoor M 2014 A review of ionic polymeric soft actuators and sensors *Soft Robot.* **1** 38–52
[10] Eisenberg A 1970 Clustering of ions in organic polymers. A theoretical approach *Macromolecules* **3** 147–54
[11] Li J Y and Nemat-Nasser S 2000 Micromechanical analysis of ionic clustering in nafion perfluorinated membrane *Mech. Mater.* **32** 303–14
[12] Hsu W Y, Gierke T D and Gierke T D 1982 Elastic theory for ionic clustering in perfluorinated ionomers *Macromolecules* **15** 101–5
[13] Datye V K, Taylor P L and Hopfinger A J 1984 Simple model for clustering and ionic transport in ionomer membranes *Macromolecules* **17** 1704–8
[14] Zhu Z, Chen H, Chang L and Li B 2011 Dynamic model of ion and water transport in ionic polymer-metal composites *AIP Adv.* **1** 040702
[15] Roth R and Gillespie D 2005 Physics of size selectivity *Phys. Rev. Lett.* **95** 9–12
[16] Minton G 2013 *Modelling the Static and Dynamic Behaviour of Electrolytes: A Modified Poisson-Nernst-Planck Approach* University of Manchester
[17] Nemat-Nasser S and Wu Y 2003 Comparative experimental study of ionic polymer-metal composites with different backbone ionomers and in various cation forms *J. Appl. Phys.* **93** 5255–67
[18] Eigen M and Wicke E 1954 The thermodynamics of electrolytes at higher concentration *J. Phys. Chem.* **58** 702–14
[19] Burak Y and Andelman D 2000 Hydration interactions: aqueous solvent effects in electric double layers *Phys. Rev.* E **62** 5296–312
[20] Spiegler K S 1958 Transport processes in ionic membranes *Trans. Faraday Soc.* **54** 1408–28
[21] Bonomo C, Fortuna L, Giannone P, Graziani S and Strazzeri S 2007 A nonlinear model for ionic polymer metal composites as actuators *Smart Mater. Struct.* **16** 1–12
[22] Madden J D W, Vandesteeg N A, Anquetil P A, Madden P G A, Takshi A, Pytel R Z, Lafontaine S R, Wieringa P A and Hunter I W 2004 Artificial muscle technology: physical principles and naval prospects *IEEE J. Ocean. Eng.* **29** 706–28
[23] Nemat-Nasser S and Li J Y 2000 Electromechanical response of ionic polymer-metal composites *J. Appl. Phys.* **87** 3321–31
[24] Cha Y and Porfiri M 2014 Mechanics and electrochemistry of ionic polymer metal composites *J. Mech. Phys. Solids* **71** 156–78
[25] Porfiri M, Sharghi H and Zhang P 2018 Modeling back-relaxation in ionic polymer metal composites: the role of steric effects and composite layers *J. Appl. Phys.* **123** 014901
[26] Bahramzadeh Y and Shahinpoor M 2011 Dynamic curvature sensing employing ionic-polymer-metal composite sensors *Smart Mater. Struct.* **20** 094011
[27] Branco P J C and Dente J A 2006 Derivation of a continuum model and its electric equivalent-circuit representation for ionic polymer-metal composite (IPMC) electromechanics *Smart Mater. Struct.* **15** 378–92

[28] Bonomo C, Fortuna L, Giannone P, Graziani S and Strazzeri S 2006 A model for ionic polymer metal composites as sensors *Smart Mater. Struct.* **15** 749–58
[29] Porfiri M 2009 An electromechanical model for sensing and actuation of ionic polymer metal composites *Smart Mater. Struct.* **18** 015016
[30] Aureli M and Porfiri M 2013 Nonlinear sensing of ionic polymer metal composites *Contin. Mech. Thermodyn.* **25** 273–310
[31] de Gennes P G, Okumura K, Shahinpoor M and Kim K J 2000 Mechanoelectric effects in ionic gels *Europhys. Lett.* **50** 513–8
[32] Schicker D and Wallmersperger T 2013 Modeling and simulation of the chemo-electro-mechanical behavior of ionic polymer-metal composites *J. Appl. Phys.* **114** 163709
[33] Zhu Z, Asaka K, Chang L, Takagi K and Chen H 2013 Multiphysics of ionic polymer-metal composite actuator *J. Appl. Phys.* **114** 084902
[34] Paquette J W, Kim K J, Nam J-D and Tak Y S 2003 An equivalent circuit model for ionic polymer-metal composites and their performance improvement by a clay-based polymer nano-composite technique *J. Intell. Mater. Syst. Struct.* **14** 633–42
[35] Olsen Z J and Kim K J 2018 A reduced dimensional mapping approach for modeling IPMCs with computational efficiency and rapid design development applications *Smart Mater. Struct.* **27** 125012
[36] Cha Y, Aureli M and Porfiri M 2012 A physics-based model of the electrical impedance of ionic polymer metal composites *J. Appl. Phys.* **111** 124901
[37] Wallmersperger T, Kröplin B and Gülch R W 2004 Coupled chemo-electro-mechanical formulation for ionic polymer gels—-numerical and experimental investigations *Mech. Mater.* **36** 411–20
[38] Pugal D, Kim K J and Aabloo A 2011 An explicit physics-based model of ionic polymer-metal composite actuators *J. Appl. Phys.* **110** 084904
[39] Rossi M and Wallmersperger T 2018 Thermodynamically consistent three-dimensional electrochemical model for polymeric membranes *Electrochim. Acta* **283** 1323–38
[40] Wallmersperger T, Horstmann A, Kroplin B and Leo D J 2009 Thermodynamical modeling of the electromechanical behavior of ionic polymer metal composites *J. Intell. Mater. Syst. Struct.* **20** 741–50
[41] Nardinocchi P, Pezzulla M and Placidi L 2011 Thermodynamically based multiphysic modeling of ionic polymer metal composites *J. Intell. Mater. Syst. Struct.* **22** 1887–97
[42] Galante S, Lucantonio A and Nardinocchi P 2013 The multiplicative decomposition of the deformation gradient in the multiphysics modeling of ionic polymers *Int. J. Non. Linear. Mech.* **51** 112–20
[43] Shams A, Lopresto V and Porfiri M 2017 Modeling fluid-structure interactions during impact loading of water-backed panels *Compos. Struct.* **171** 576–90
[44] Olsen Z J and Kim K J 2021 A hyperelastic porous media framework for ionic polymer-metal composite actuators and sensors: thermodynamically consistent formulation and nondimensionalization of the field equations *Smart Mater. Struct.* **30** 095024
[45] Leronni A and Bardella L 2021 Modeling actuation and sensing in ionic polymer metal composites by electrochemo-poromechanics *J. Mech. Phys. Solids* **148** 104292
[46] Shen Q, Palmre V, Stalbaum T and Kim K J 2015 A comprehensive physics-based model encompassing variable surface resistance and underlying physics of ionic polymer-metal composite actuators *J. Appl. Phys.* **118** 124904
[47] Wallmersperger T, Leo D J and Kothera C S 2007 Transport modeling in ionomeric polymer transducers and its relationship to electromechanical coupling *J. Appl. Phys.* **101** 024912
[48] Olsen Z J 2021 A hyperelastic porous media framework for ionic polymer-metal composites and characterization of transduction phenomena via dimensional analysis and nonlinear regression *UNLV Theses, Diss. Prof. Pap. Capstones* University of Nevada, Las Vegas (May)
[49] Corless R M, Gonnet G H, Hare D E G, Jeffrey D J and Knuth D E 1996 On the Lambert W function *Adv. Comput. Math.* **5** 329–59
[50] Mccabe B J H 1983 *The Quotient-Difference Algorithm and the Padé Table: An Alternative Form and a General Continued Fraction* pp 183–97
[51] Porfiri M 2008 Charge dynamics in ionic polymer metal composites *J. Appl. Phys.* **104** 104915
[52] Nardinocchi P and Pezzulla M 2013 Curled actuated shapes of ionic polymer metal composites strips *J. Appl. Phys.* **113** 224906